Direct numerical simulation of a two-way thermally coupled droplet-laden mixing layer

By WEI LING[1], J. N. CHUNG[2] AND C. T. CROWE[1]

[1]School of Mechanical and Materials Engineering, Washington State University, Pullman, WA 99164, USA

[2]Department of Mechanical Engineering, University of Florida, Gainesville, FL 32611, USA

Because the three-dimensional large-scale vortex structures dominate the dispersion of particles at intermediate Stokes numbers in shear layers, there is interest in understanding the two-way thermal coupling effect in droplet–gas flows for practical combustion applications. Using pseudo-spectral and Lagrangian approaches, three-dimensional two-way thermally coupled droplet-laden mixing layers are studied with hot air and cool water droplets. Higher air density is observed around the region of the interface of the two streams and, thus, thermal contraction occurs in this region. This thermal contraction results in an increase of the magnitude of the vorticity field, a more unstable flow, a higher droplet concentration and a lower droplet dispersion across the mixing layer.

1. Introduction

The dispersion of particles under the effect of large-scale turbulence in shear layers has been of interest for the past twenty years. The large-scale organized spanwise vortex structures in two-dimensional mixing layers have been identified and studied both numerically and experimentally (Ho & Huerre 1984). Extensive numerical and experimental studies have also been carried out to examine particle dispersion by the two-dimensional organized vortex structures. It has been found that these vortex structures have a dominant effect on the dispersion of particles over a range of Stokes numbers (Eaton & Fessler 1994; Crowe, Chung & Troutt 1988; Chung & Troutt 1988; Crowe, Troutt & Chung 1996).

Although the two-dimensional large vortex structures are very stable, they are still subject to three-dimensional instabilities. The three-dimensionality of the plane mixing layer has been observed and studied not only in experiments (Miksad 1972; Breidenthal 1978; Browand & Troutt 1980; Wygnanski *et al.* 1979; Lasheras, Cho & Maxworthy 1986; Lasheras & Choi 1988; Huang & Ho 1990), but also in numerical simulations. The counter-rotating 'rib' vortices, which exist in the region between the rollers (the braid region) and extend from the bottom of one roller to the top of the next, were found in most numerical simulations. The wavelength of the three-dimensional instability was found to be about two-thirds of the wavelength of the two-dimensional instability (Pierrehumbert & Widnall 1982). The small-scale three-dimensional instabilities were shown to exist in free shear flows at moderately low Reynolds numbers, and are responsible for the initial development of the three-dimensionality. It was also found that the pairing of the two-dimensional large-scale vortex structures has a suppressing effect on the growth rate of the

three-dimensional structures. Once the three-dimensional modes reach a finite amplitude, they manifest themselves mainly as counter-rotating, streamwise vortices that are located on the braids between the spanwise-coherent two-dimensional pairing modes, and the stabilizing effect of the two-dimensional structures is reduced (Metcalfe *et al.* 1987; Moser & Rogers 1993).

Then a question arises: How do the three-dimensional large-scale structures affect the dispersion of particles? Marcu & Meiburg (1996) investigated the features of particle dispersion in a three-dimensional temporal mixing layer without vortex pairing. The presence of the streamwise vortices results in additional dynamic effects that modify the dispersion patterns of particles. Intense three-dimensional vortex stretching and folding produces 'mushroom'-shaped particle dispersion patterns. Tong & Wang (1997) also studied a three-dimensional particle-laden mixing layer. They used the pseudo-spectral method with a Fourier vorticity-based scheme to simulate the flow field and used both trajectory and continuum approaches to simulate the dispersion of particles with a Stokes number of unity. Ling *et al.* (1998) employed an initial three-dimensional random perturbation to simulate a three-dimensional temporal particle-laden mixing layer using the pseudo-spectral method and the Lagrangian approach. The counter-rotating rib structure developed naturally from the initial random perturbation and the strength of the streamwise vorticity is about one-tenth of that of the spanwise vorticity. Particles with Stokes number of the order of unity were still found to have the largest concentration on the circumference of the two-dimensional large-scale structures. The presence of the streamwise large-scale structures causes the variation of the particle concentrations along the spanwise and the transverse directions. The extent of variation also increases with the development of the three-dimensionality, which results in the mushroom-shaped particle distribution.

The dispersion of particles in turbulence is important in industrial applications such as combustion, pollution control and materials processing. One of the applications of the non-uniform concentration of particles is in the combustion of particulate fuels or injected liquid fuel. The overall stoichiometry may be very lean but quite fuel-rich environments can occur in the high strain region due to the demixing effect. Higher combustion efficiency and lower pollution generation can be achieved by controlling the preferential concentration. The above simulations are based on one-way coupling, i.e. only the flow affects the dispersion of particles. However, moderate mass loadings of particles can alter the fluid flow and for any non-isothermal flow (such as any combustion process), the evaporating droplets represent mass sources and thermal sinks in the flow. For turbulence modulation in particle-laden flows, Gore & Crowe (1991) reviewed the available experimental data and proposed that the ratio of particle diameter to the length scale of the most energetic eddy is a good indicator. Squires & Eaton (1990) and Boivin, Simonin & Squires (1998) studied forced homogeneous isotropic stationary particle-laden turbulence and Elghobashi & Truesdell (1993) investigated a decaying isotropic particle-laden turbulent flow with particles. They have found that particles increase the turbulent kinetic energy at high wavenumbers and decrease it at low wavenumbers. An experimental effort has also been made to investigate the kinetic energy transfer in a two-phase turbulent shear flow and an inhomogeneous transfer of kinetic energy between the phases was also found (Kiger & Lasheras 1995).

Saffman (1962), Tatsumi, Gotoh & Ayukawa (1964), Michael (1965), Yang *et al.* (1990), and Tong & Wang (1998*a*) studied the linear stability of the two-way momentum-coupled particle-laden mixing layer using the Orr–Sommerfeld equation.

It was found that the addition of particles with small Stokes number destabilizes the flow while the addition of particles with moderate and large Stokes numbers stabilizes the flow. Particles with Stokes number of order of unity have the most stabilizing effect on the linear stability of the flow. Concerning the effect of the presence of the particles on the large-scale vortex structures of the mixing layer, Tang *et al.* (1989) reported the results of a numerical study on the effect of momentum coupling on a two-dimensional temporal mixing layer. They used the discrete vortex method and the viscous flow effects were neglected based on the assumption of high Reynolds number. It was found that the effect of momentum coupling is to delay the vortex development process without noticeably affecting the mechanisms for the vortex growth. Continuing their linear stability analysis, Tong & Wang (1998*b*) also studied the momentum coupling effect on a two-dimensional temporal mixing layer. They also found that the particle-laden mixing layer has the same rollup and pairing processes as the single-phase mixing layer. However the time scales and length scales were found to be larger and segregation of the vortex structures can result due to the forcing from the momentum coupling terms for particles at intermediate Stokes number.

Effort has also been devoted to numerical simulations of two-way-coupled droplet-laden turbulent flows. Berlemont, Grancher & Gouesbet proposed mass, momentum and heat source terms due to the phase change of droplets for the (k–ϵ) model and simulated methyl alcohol droplets in a heated turbulent round jet. Using a direct numerical simulation technique, Mashayek (1998*a*) investigated two-way mass, momentum and energy coupling effects on droplet-laden low-Mach-number homogeneous shear flows. It was found that while the presence of non-evaporating droplets decreases the turbulent kinetic energy of the flow, droplet evaporation increases both the turbulent kinetic energy and the mean internal energy of the flow by mass transfer. He also studied the dispersion of evaporating droplets in a forced low-Mach-number isotropic turbulent flow (Mashayek 1998*b*). Xu *et al.* (1998) used the discrete vortex method to study a two-dimensional droplet-laden wake flow with mass and thermal energy coupling. They found that increasing mass or thermal coupling reduces the dispersion of droplets and a large value of either of the two coupling parameters results in a breakdown of the coherent vortex structures. However, there are no published results on two-way thermal energy coupling effects on a three-dimensional droplet-laden mixing layer.

The objective of present study is to investigate the two-way thermal energy coupling effect on both the large-scale vortex structures of a three-dimensional temporal mixing layer and the dispersion of droplets. Section 2 provides the governing equations for the simulations and describes the numerical methods for the simulations. The simulation results are discussed in §3 and a summary of this study is presented in §4. The Appendix contains the detailed derivation of the approximated thermal equation for the continuous phase.

2. Numerical modelling

2.1. *Governing equations*

The simulations of the two-way thermal energy coupling effect are performed for cool water droplets in hot air such that the droplets are treated as thermal sinks in the flow. The following assumptions are made to simplify the problem:

(i) The volume fraction of the droplets is very small ($< 10^{-3}$) and the mass

loading is low (< 0.1) such that the continuous phase is treated as ideal gas with the properties of air.

(ii) The Mach number is low. Under this assumption, the kinetic energy associated with the mass transfer and the work rate associated with the drag force are neglected because both are scaled by the Eckert number, which is proportional to the square of the Mach number (Crowe, Sommerfeld & Tsuji 1997).

(iii) The conductive heat transfer through the mixture is neglected due to the large Péclet number, which is of the same order as the Reynolds number for a dilute gas–droplet mixture.

(iv) All droplets are spheres with identical initial diameter D_0 and density ρ_d and they are approximated as heat sinks in the air flow.

(v) The material density of the droplets is much larger than that of the air.

(vi) Droplet–droplet interactions are neglected based on the dilute two-phase flow assumption.

(vii) Gravity is neglected for both phases.

(viii) Initially, the droplets are in dynamic equilibrium with the mean flow and at the wet-bulb temperature, T_{wb}.

The accuracy of point-source assumption was examined in detail in the paper by Eaton & Rouson (1998). They compared the results of using this assumption with those of fully modelled particles. They concluded that as long as the diameter of the particles is small compared to the grid scale of the computational cell, the point-source assumption is reasonably valid. In one of their test cases where they found the point-source assumption to be acceptable, 64 000 particles with diameters of 70 microns and 11% mass loading were simulated in a $32 \times 65 \times 32$ grid system. The diameter to grid spacing ratio is approximately 0.25. In present simulations, 262 144 particles with only 6% mass loading were put in a $128 \times 129 \times 128$ grid system. The diameter to grid spacing ratio is around 0.12 which is smaller than that in the acceptable case of Eaton & Rouson (1998). Therefore, the point-source assumption in the present study is reasonable.

Based on the above assumptions, the non-dimensional state equation of an ideal gas, and conservation equations of mass, momentum and thermal energy for the continuous phases can be simplified to following equations:

$$P_0' = \rho_c' T_c', \tag{2.1}$$

$$\frac{\partial \rho_c'}{\partial t'} + \frac{\partial (\rho_c' U_i')}{\partial x_i'} = 0, \tag{2.2}$$

$$\frac{\partial (\rho_c' U_i')}{\partial t'} = -\frac{\partial P'}{\partial x_i'} + \frac{1}{Re}\frac{\partial^2 U_i'}{\partial x_j' \partial x_j'} - \frac{\partial (\rho_c' U_i' U_j')}{\partial x_j'}, \tag{2.3}$$

$$\frac{\partial T_c'}{\partial t'} = \frac{1}{\rho_c'}\left(-(\gamma-1)P_0'\frac{\partial U_i'}{\partial x_i'} + \gamma S_h'\right) - U_i'\frac{\partial T_c'}{\partial x_i'}, \tag{2.4}$$

where superscript prime denotes a non-dimensional term, subscript c denotes the properties of the continuous phase, $\gamma = C_p/C_v$, Re is the Reynolds number of the flow based on the velocity scale, length scale, and the kinematic viscosity of the fluid, and S_h' is the thermal energy coupling term.

The equations are non-dimensionalized by initial air density ρ_0, initial air temperature T_0, the velocity scale U_0, which is the velocity difference between the two parallel streams of the mixing layer, and the length scale L_0, which is equal to $\lambda_x/2\pi$. Here, λ_x

is the most unstable streamwise wavelength and is determined by the initial vorticity thickness which depends on the initial mean velocity profile.

Due to the low Mach number assumption, the ambient pressure P_0, which is only a function of time (see discussion in the Appendix), is included in the equation of state relating gas density to temperature. The mass and momentum coupling effects are neglected due to the low initial mass loading. However, the energy transfer which is associated with latent heat can become important. The simiplication process for the thermal energy equation is shown in the Appendix.

The non-dimensional thermal energy coupling term S_h' in equation (2.4) is defined as

$$S_h' = \sum_k^N S_{hk}' = \sum_k^N \frac{\tilde{\rho}_d' Nu}{3 St Pr}(T_{wb}' - T_d'),\qquad(2.5)$$

where N is the total number of droplets in the control volume, $\tilde{\rho}_d'$ is the local bulk density of the kth droplet, and T_d' the air temperature at the position of the kth droplet.

St, the Stokes number of a droplet, is defined as

$$St = \frac{\rho_d D^2/(18\mu)}{L_0/U_0},\qquad(2.6)$$

where μ is the viscosity of the continuous phase and D is the diameter of the droplet.

Nu, the Nusselt number, is related to the relative Reynolds number and Prandtl number by

$$Nu = 2 + 0.6 Re_r^{0.5} Pr^{0.33},\qquad(2.7)$$

where $Pr = \mu C_p/K_c$ with K_c the thermal conduction coefficient. Re_r is the droplet relative Reynolds number, which is based on the diameter of the droplet, the speed difference between the droplet and the local flow, and the kinematic viscosity of the continuous phase. In the present study, Re_r is less than 3 for all cases.

To simplify the problem, all droplets are assumed to be initially at the wet-bulb temperature, so the temperature of the droplets is constant. The reason for the simplification is as follows. From the analysis of Crowe *et al.* (1997), the droplet thermal response time (the time scale associated with the droplet heating-up stage) is of the same order of magnitude as the droplet momentum response time for a gas flow. So, at a Stokes number of order of unity, the non-dimensional thermal response time of the droplets is also of the order of unity. From the previous one-way coupling study (Ling *et al.* 1998), the three-dimensional large-scale vortex structures are only fully developed around non-dimensional times of 30, which is much larger than the droplet thermal response time. Therefore, the evaporation stage is much more important than the heating-up stage.

Using equations (2.1) and (2.2), one can rewrite the thermal energy equation as

$$\frac{\mathrm{d}P_0'}{\mathrm{d}t'} = -\gamma P_0' \frac{\partial U_i'}{\partial x_i'} + \gamma S_h'.\qquad(2.8)$$

Integrating equation (2.8) and using the periodic and free-slip boundary conditions, one obtains the equation for P_0':

$$\frac{\mathrm{d}P_0'}{\mathrm{d}t'} = \frac{1}{V} \iiint \gamma S_h' \mathrm{d}v,\qquad(2.9)$$

where V is the volume of the domain.

The non-dimensional motion equation for a droplet is

$$\frac{\mathrm{d}V'}{\mathrm{d}t'} = \frac{f}{St}(U' - V'), \tag{2.10}$$

where V' is the velocity of a droplet, U' is the velocity of fluid at the position of the droplet and f is a modification factor for the non-Stokes effect (Ling *et al.* 1998).

Due to the evaporation, the size of the droplet changes with time according to the non-dimensional equation

$$(D'^{(n+1)})^2 = (D'^{(n)})^2 - \lambda \Delta t', \tag{2.11}$$

where λ, the non-dimensional droplet evaporation parameter, is calculated at each time step for every droplet using the following approximation:

$$\lambda \approx \frac{4Nu}{PrRe\rho_d'} \frac{T_0 C_p}{h_L}(T_d' - T_{wb}'), \tag{2.12}$$

where ρ_d' is the non-dimensionalized droplet density, C_p is the specific heat and h_L is the latent heat.

2.2. *Numerical procedure*

The numerical procedure consists of the following three steps. The first step is to compute the thermodynamic field of the continuous phase. The temperature field and the pressure P_0' are first advanced in time using the second-order Adam–Bashforth scheme according to equations (2.4) and (2.9). The density field is then obtained by using the following non-dimensional equation:

$$\rho_c' = \frac{P_0'}{T_c'}. \tag{2.13}$$

The second step is to compute the dynamics of the continuous phase. First, the second-order Adam–Bashforth scheme is used to advance the product of the density and velocity of the continuous phase to an intermediate time step without the effect of the pressure gradient:

$$(\rho_c' U_i')^{(n+1/2)} = (\rho_c' U_i')^{(n)} + \Delta t'(\tfrac{3}{2}B_i^{(n)} - \tfrac{1}{2}B_i^{(n-1)}), \tag{2.14}$$

where

$$B_i = \frac{1}{Re}\frac{\partial^2 U_i'}{\partial x_j' \partial x_j'} - \frac{\partial(\rho_c' U_i' U_j')}{\partial x_j'}. \tag{2.15}$$

Then, $(\rho_i' U_i')^{(n+1/2)}$ is corrected by considering the pressure effect:

$$\frac{(\rho_c' U_i')^{(n+1)} - (\rho_c' U_i')^{(n+1/2)}}{\Delta t'} = -\frac{\partial P'^{(n+1)}}{\partial x_i'}. \tag{2.16}$$

Taking the divergence of (2.16) and using the continuity equation, one obtains the Poisson equation for the pressure:

$$\frac{\partial^2 P'^{(n+1)}}{\partial x_i' \partial x_i'} = \frac{1}{\Delta t'}\left(\frac{\partial \rho_c'^{(n+1)}}{\partial t'} + \frac{\partial(\rho_c' U_i')^{(n+1/2)}}{\partial x_i'}\right), \tag{2.17}$$

where the term $\partial \rho_c'^{(n+1)}/\partial t'$ is approximated by $(\rho_c'^{(n+1)} - \rho_c'^{(n)})/\Delta t'$.

Finally, the third step is to compute the dispersed phase and the thermal energy

Case	T_0 (K)	T_{wb} (K)	T'_{wb}	St_{mass}
TE600	384.5	306.2	0.796	600
TE800	360.2	301.2	0.836	800
TE1000	345.0	297.5	0.862	1000

TABLE 1. Two-way thermal coupling cases.

coupling terms introduced by the evaporation. The velocity and position of a droplet can be obtained by integrating equation (2.10):

$$V'^{(n+1)} = U' + (V'^{(n)} - U') \exp\left(-\frac{f \Delta t'}{St}\right), \tag{2.18}$$

$$X_p'^{(n+1)} = X_p'^{(n)} + U' \Delta t' + (V'^{(n)} - U') \frac{St}{f}\left(1 - \exp\left(-\frac{f \Delta t'}{St}\right)\right), \tag{2.19}$$

where the fluid velocity U' and f are taken as constants during the integration over a very small time step size.

Because one only has the velocity of the flow field at every grid point, the third Lagrange interpolating polynomial is used to obtain the flow velocities at the positions of the droplets. Other methods for evaluating the flow velocity are discussed by Balachandar & Maxey (1989).

Using the pseudo-spectral method, the non-dimensionalized air density ρ'_c, air velocities U'_i, air pressure P', and temperature T'_c are represented by finite Fourier series and all the spatial derivatives are solved in spectral space.

The initialization of the flow velocity field consists of two parts. One is the mean velocity field and the other is the perturbations to the mean. The initial mean velocity field is given as the hyperbolic tangent function of the transverse direction only. The initial perturbations also consist of two parts. The first part is the initial two-dimensional perturbation, which is imposed on the two-dimensional fundamental and subharmonic unstable wavenumbers, derived from the linear Orr–Sommerfeld equations (Michalke 1964). The second part is the initial three-dimensional perturbation which is a specific energy spectrum with random fluctuating components. For the details of the initialization, see Ling *et al.* (1998).

3. Simulation results

For the present study, the Reynolds number is 500, the initial Stokes number of droplets is 4, the density ratio of the water to the air is 1000 and the air is at an initial pressure of 1 bar with $Pr = 0.68$. Table 1 shows the other parameters for the three two-way thermal coupling cases. St_{mass}, the non-dimensional droplet mass response time, is defined as

$$St_{mass} = \frac{(D'_0)^2}{\lambda_0} \tag{3.1}$$

where λ_0 is the initial value of λ and D'_0 is the initial diameter of the droplet.

A higher St_{mass} means a higher T'_{wb}, thus lower thermal coupling effects. The size of the computational box is $4\pi \times 4\pi \times 4\pi$ with $128 \times 129 \times 128$ grids. $128 \times 8 \times 128$ droplets are uniformly seeded in the region $|Y| < \pi/4$ initially and they are initially in dynamic equilibrium with the mean flow. The initial mass loading for all the three
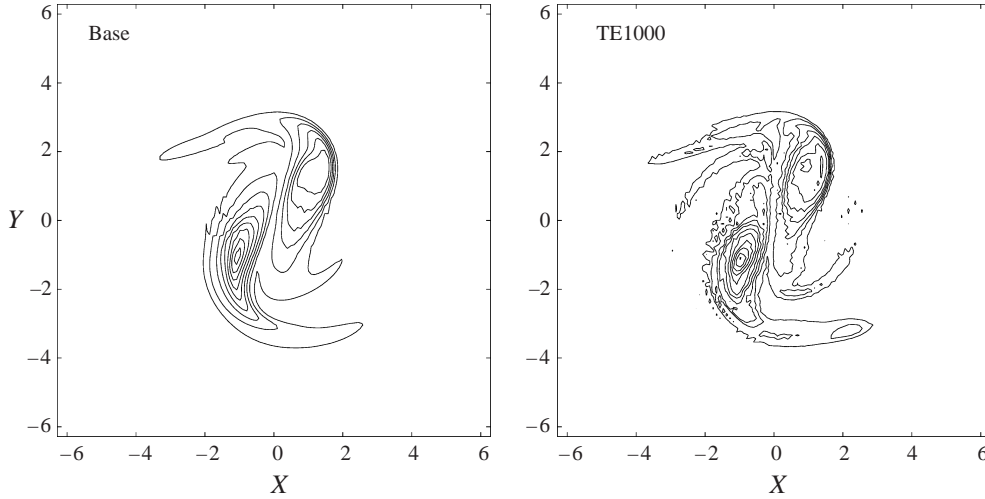
FIGURE 1. Contours of the spanwise vorticity at $Z = 0$ and $T = 24$.

cases is about 0.06. A base case is also simulated to be compared with all the three two-way thermal coupling cases. For the base case, there is no heat transfer between the two phases and the initial dynamic field for both phases is the same as mentioned above.

The simulation results for the dynamics of the vorticity, the thermodynamic field and the properties of the droplets are discussed in the following three subsections. All the properties or variables are in their dimensionless form. The superscript primes for all terms are droped for simplification. T is used to represent non-dimensional time.

3.1. *Vorticity dynamics*

The vorticity dynamics, especially the development of the Kelvin–Helmholtz rollups, the vortex pairing, and the counter-rotating rib structures are studied in this section.

By taking curl of equation (2.3), one obtains the vector form of the vorticity equation:

$$\frac{\mathrm{D}\boldsymbol{\omega}}{\mathrm{D}t} + \boldsymbol{\omega}\nabla \cdot \boldsymbol{U} = \frac{1}{\rho_c^2}(\nabla\rho_c \times \nabla P) + \frac{1}{Re}\nabla \times \left(\frac{\nabla^2 \boldsymbol{U}}{\rho_c}\right) \tag{3.2}$$

where $\boldsymbol{\omega}$ is the vorticity vector of the flow. The heat sinks caused by the evaporation of the droplets can result in not only a change of the air density field, which then results in a change of the vorticity field, but also in the baroclinical torque, the first term on right-hand side of the vorticity equation, due to the misalignment of density gradient and pressure gradient.

The contours of the spanwise vorticity at $Z = 0$ (figure 1) and the streamwise vorticity at $X = -L_x/2$ (figure 2) and $X = 0$ (figure 3) for case TE1000 are compared with those for the base case at $T = 24$. The large-scale vortex structures, such as the vortex pairing and the counter-rotating ribs, are almost the same as for the base case. However, the cooler droplets near $Y = 0$ provide a heat sink for the surrounding air. The cooling of the air causes an increase in the local air density and thus a contracting effect which is called 'thermal contraction'. The contraction of the flow then results in a higher magnitude of the vorticity because of the conservation of the angular momentum of the fluid. On the other hand, it was shown by McMurtry,
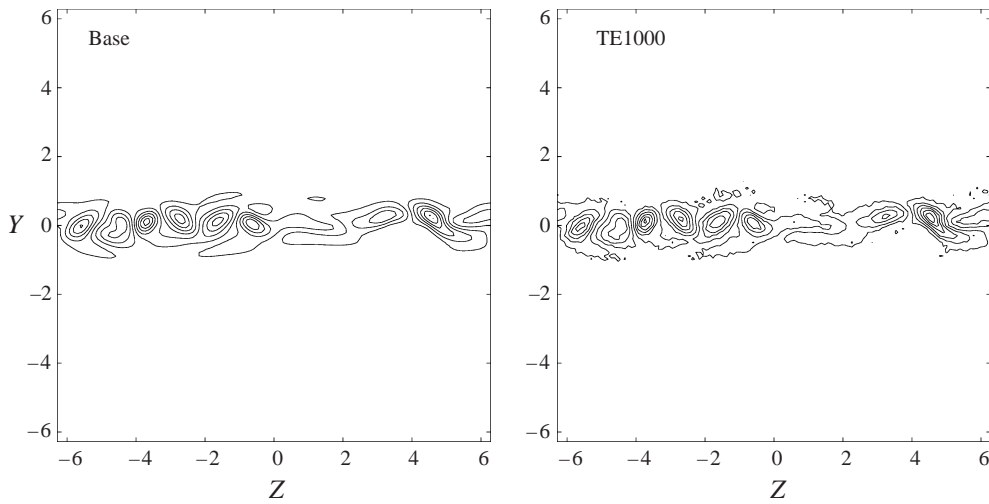
FIGURE 2. Contours of the streamwise vorticity at $X = -L_x/2$ and $T = 24$.
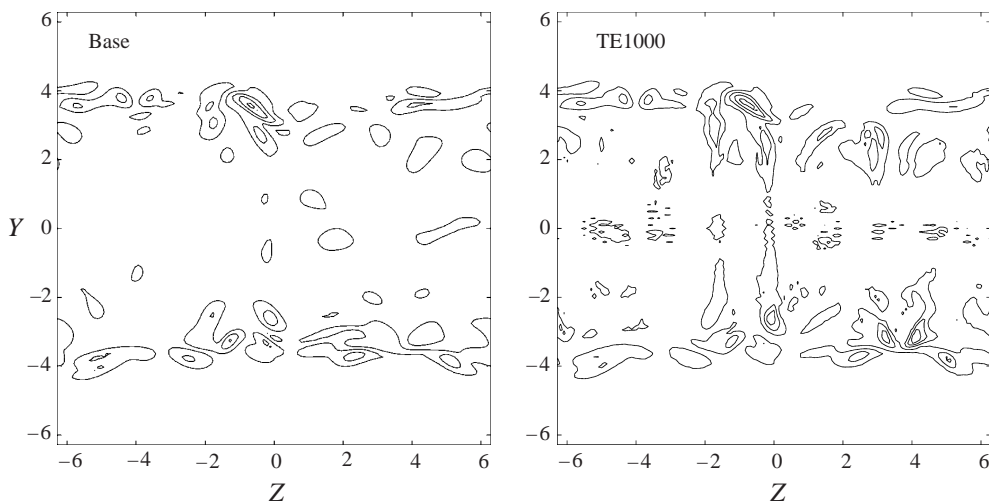
FIGURE 3. Contours of the streamwise vorticity at $X = 0$ and $T = 24$.

Riley & Metcalfe (1989) that the vorticity magnitude is reduced due to the expansion of the flow in a mixing layer with heat release from chemical reaction.

The development of the total magnitude of the baroclinical torques in the spanwise and streamwise directions are shown in figure 4 for cases TE1000 and TE800. It is shown that the magnitude of the baroclinical torque in the spanwise direction is one order of magnitude larger than that in the streamwise direction and the torque in the spanwise direction reaches a local maximun value around the vortex pairing time. Figure 5 shows the contours of baroclinical torque in the spanwise direction in the $Z = 0$ plane and in the streamwise direction in the $X = 0$ plane. It is shown that the baroclinical torque is distributed on the circumference of the large-scale vortex structures and is of small scale. The distribution of the baroclinical torque seems to be determined by the distribution of droplets, which determines the local density
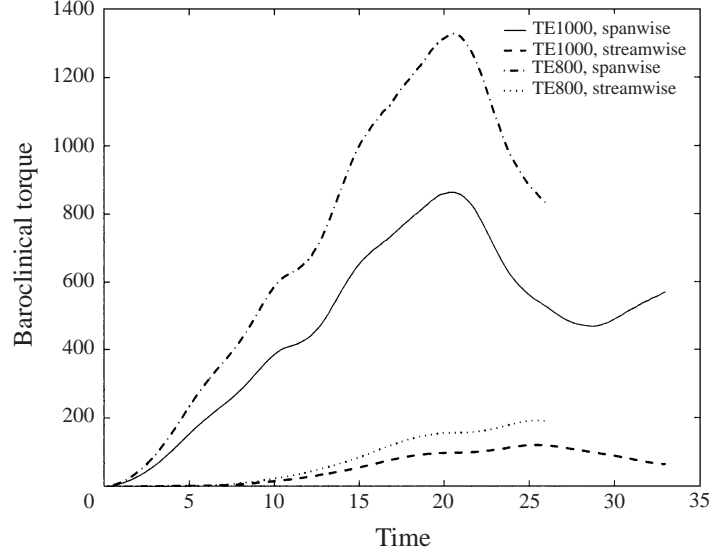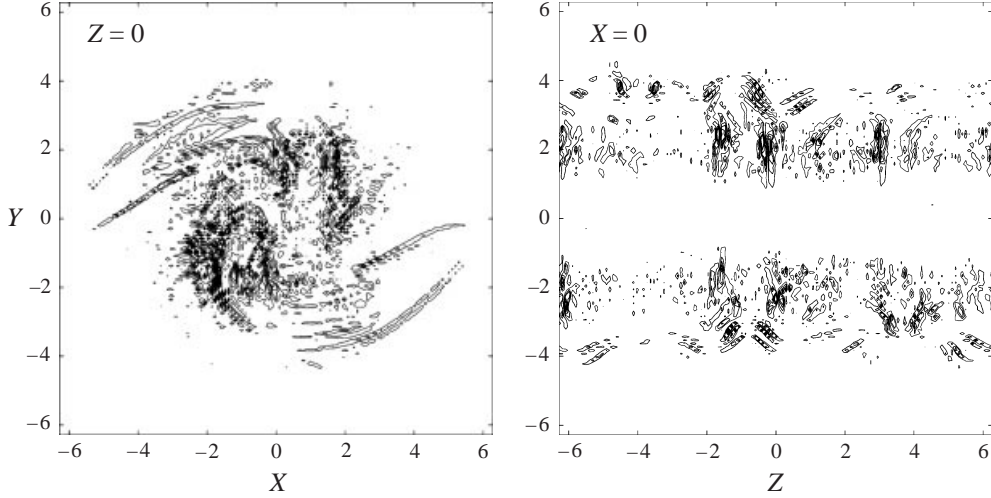
FIGURE 4. Development of baroclinical torque.

FIGURE 5. Contours of the baroclinical torque at $T = 24$.

gradient. The small-scale baroclinical torque can result in less-smooth contours of the vorticity field when compared with the base case.

The increase in the magnitude of the vorticity can also be shown in the development of the total magnitudes of the spanwise vorticity $|\omega_z|_T$ and the streamwise vorticity $|\omega_x|_T$. Here, $|\omega_z|_T$ and $|\omega_x|_T$ are defined as

$$|\omega_z|_T = \sum_x \sum_y \sum_z \omega_z^2(x, y, z), \qquad (3.3)$$

$$|\omega_x|_T = \sum_x \sum_y \sum_z \omega_x^2(x, y, z), \qquad (3.4)$$

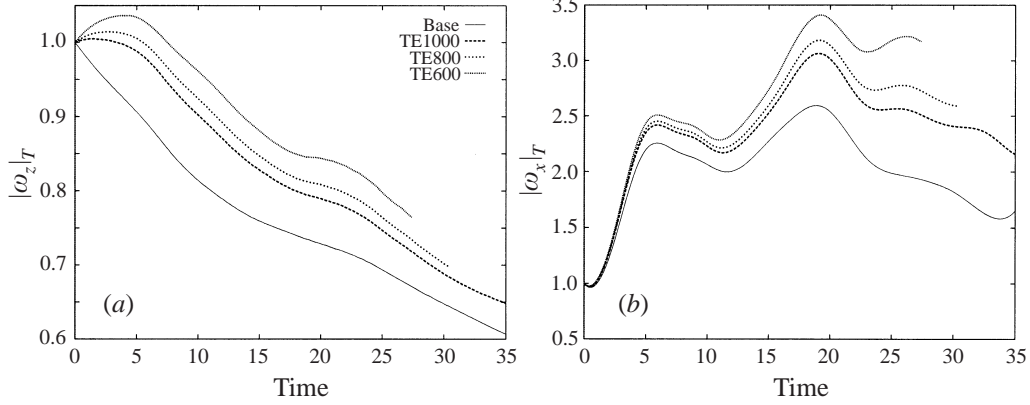where ω_z is the spanwise vorticity and ω_x is the streamwise vorticity.

FIGURE 6. Development of the total magnitude of (*a*) spanwise vorticity and (*b*) streamwise vorticity, normalized by their initial values.
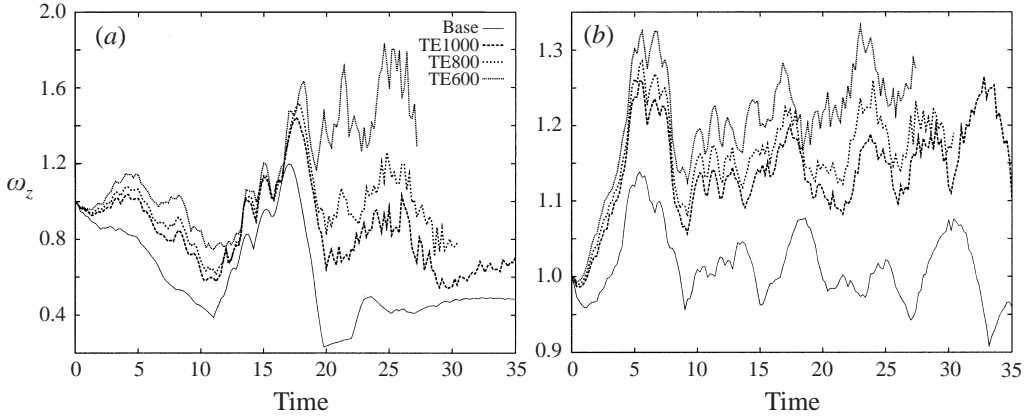

FIGURE 7. Development of (*a*) maximum and (*b*) minimum value of ω_x normalized by its initial value.

The development of $|\omega_z|_T$ and $|\omega_x|_T$ normalized by their initial values is shown in figures 6(*a*) and 6(*b*) for the three two-way coupling cases as well as the base case. It is observed that a case with a higher thermal energy coupling effect has higher values of $|\omega_z|_T$ and $|\omega_x|_T$.

While the normalized value of $|\omega_z|_T$ decreases as time increases for the base case, it initially increases with time for the other three cases. The reasons are as follows: For the base case, the spanwise vorticity initially concentrates in the narrow region around $Y = 0$. As the flow develops, the spanwise vorticity starts to be redistributed to a broader region. This results in a lower value of $|\omega_z|_T$ because the circulation is conserved. However, for the cases with evaporation of droplets, because initially droplets are uniformly seeded in the very narrow region around $Y = 0$, the effect of the thermal contraction, at its highest degree, causes the spanwise vorticity to concentrate in a narrower region and thus results in an increase of $|\omega_z|_T$. As the flow develops, the droplets are thrown out by the large-scale vortex structures. So the vorticity is able to be redistributed to regions of higher $|Y|$. Therefore, after $T \simeq 7$, which is approximately the rollup time, the normalized value of $|\omega_z|_T$ for all the three cases behaves similarly to the base case.
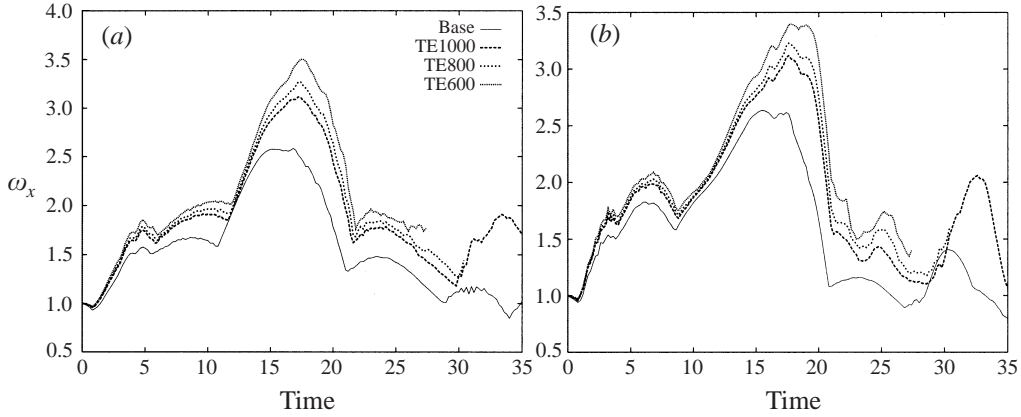
FIGURE 8. Development of (*a*) maximum and (*b*) minimum value of ω_x normalized by its initial value.

The increase in the magnitude of the vorticity can also been seen in figures 7 and 8, which display the development of the maximum and minimum values of ω_z and ω_x normalized by their respective initial values. Because the minimum values of ω_z and ω_x for all cases are negative, the normalized values represent the magnitude of the minimum values. It is again observed that the case with a larger thermal coupling effect results in a higher magnitude of the vorticity due to more thermal contraction.

It has been argued that the strength of the Kelvin–Helmholtz rollups and the vortex pairing are associated respectively with $E_{(1,0)}$, the energy in the streamwise fundamental wavenumber, and $E_{(0.5,0)}$, the energy in the streamwise subharmonic wavenumber (Ling *et al.* 1998; Tong & Wang 1998*b*). Here, $E_{(1,0)}$ and $E_{(0.5,0)}$ are defined as

$$E_{(1,0)} = \sum_{k_y} C_u \big|_{k_x=1,\,k_z=0}, \tag{3.5}$$

$$E_{(0.5,0)} = \sum_{k_y} C_u \big|_{k_x=0.5,\,k_z=0}. \tag{3.6}$$

The development of the energy in these two specific Fourier modes is shown in figures 9(*a*) and 9(*b*). It is observed that at the first peak of the energy at the fundamental mode, a case with higher thermal coupling effects has higher values due to more thermal contraction. At later times, the development of the energy in the fundamental mode for the two-way coupling cases shows a small delay, compared with the base case. The development of the energy in the subharmonic mode for the two-way coupling cases also shows a slight delay and a case with higher thermal coupling effects has a higher peak value of this energy. Again, this indicates that a case with higher thermal coupling effects has increased strength of the vortex rollups and pairing.

While a non-uniform distortion of the energy spectrum due to the two-way momentum coupling effect is observed for particle-laden turbulent flows (Elghobashi & Truesdell 1993; Squires & Eaton 1990; Boivin *et al.* 1998), a uniform increase in the energy spectrum is observed in the present simulations with two-way thermal
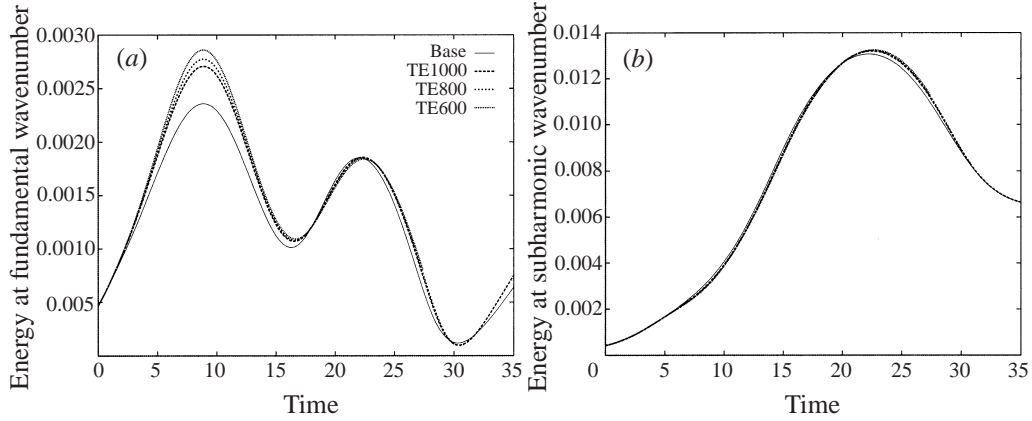
FIGURE 9. Development of (*a*) $E_{(0,1)}$ and (*b*) $E_{(0.5,0)}$ for two-way thermal energy coupling cases.
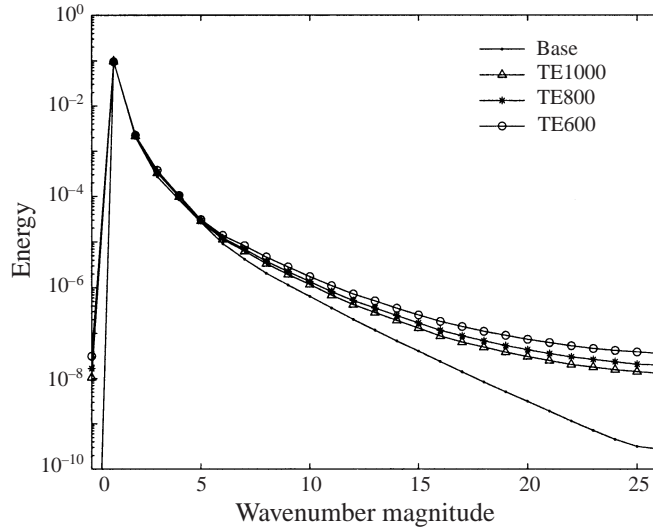
FIGURE 10. Energy spectra for two-way thermal coupling cases at $T = 25$.

coupling. The energy spectrum is defined as

$$E(k) = \begin{cases} \displaystyle\sum_{k-1 < K \leqslant k} C_u & \text{when } k \neq 0 \\ C_u \big|_{k_x=0, k_y=0, k_z=0} & \text{when } k = 0, \end{cases} \tag{3.7}$$

where $k = 0, 1, 2, \ldots$ and $K = \sqrt{k_x^2 + k_y^2 + k_z^2}$.

The energy spectra for all the cases at $T = 25$ are displayed in figure 10. It is shown that the case with higher thermal coupling effects contains more according to the energy spectrum. The energy increase is caused by the thermal contraction on both the large and small scales and it indicates a more unstable flow. This can also be shown in the development of the momentum thickness δ_m, which is defined as

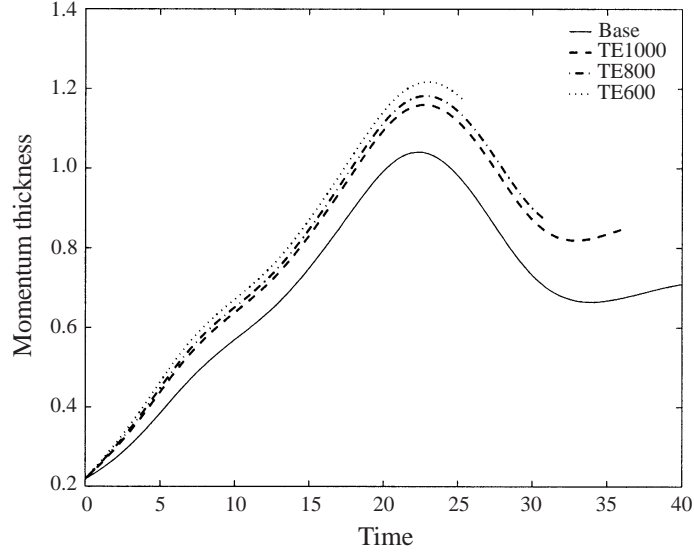$$\delta_m = \int_{-\infty}^{\infty} (0.25 - \bar{U}_1(y)^2) \, \mathrm{d}y, \tag{3.8}$$

FIGURE 11. Development of the momentum thickness.

where

$$\bar{U}_1(y) = \frac{\displaystyle\int_{-L_x/2}^{L_x/2} \int_{-L_z/2}^{L_z/2} \rho_c U_1(x, y, z)\mathrm{d}x\mathrm{d}z}{\displaystyle\int_{-L_x/2}^{L_x/2} \int_{-L_z/2}^{L_z/2} \rho_c \mathrm{d}x\mathrm{d}z}. \tag{3.9}$$

As shown in figure 11, the development of the momentum thickness reaches a local maximum value around $T = 23$ for all the cases, which corresponds to the completion of the vortex pairing. A case with larger thermal coupling effects has a larger value of momentum thickness, which indicates a higher growth rate the mixing layer.

As the heat is transferred from the hot air to the cool droplets to supply the energy needed for the droplet evaporation, lower air temperature, higher air density, or thermal contraction results. To sustain the angular momentum of the flow field, the strength of the vorticity field is increased due to the thermal contraction. As a result, the flow field becomes more unstable.

3.2. *Thermodynamic field*

The thermodynamic properties of the flow field, such as the thermodynamic pressure, air temperature, and air density, are studied in this section. All the properties are presented in their non-dimensional forms.

Figure 12 shows the evolution of the thermodynamic pressure for the cases with two-way thermal coupling effects. Because the simulations are performed for a closed domain and the low Mach number assumption is used, the thermodynamic pressure is a function of time only. According to equation (2.9), the rate of change of the thermodynamic pressure should be negative since the thermal coupling term is always negative. The decrease of the thermodynamic pressure is shown in figure 12 and the case with higher thermal coupling effect is found to have an augmented decrease rate. Over the duration of the simulation, the thermodynamic pressure has been reduced by around 10%.
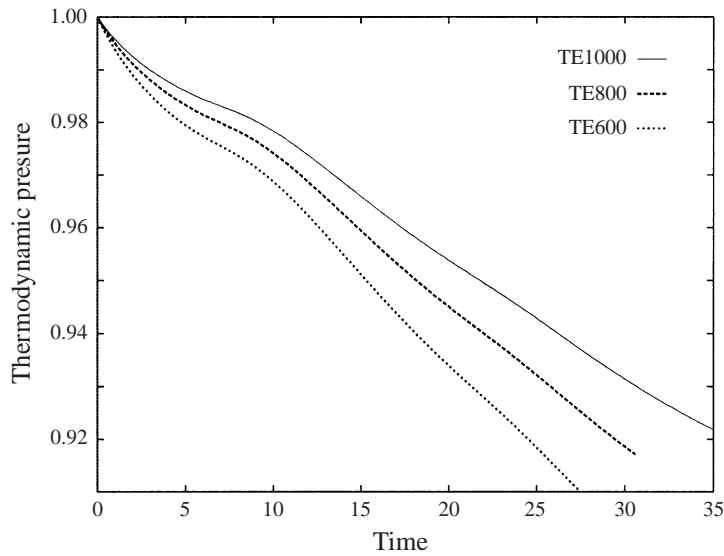
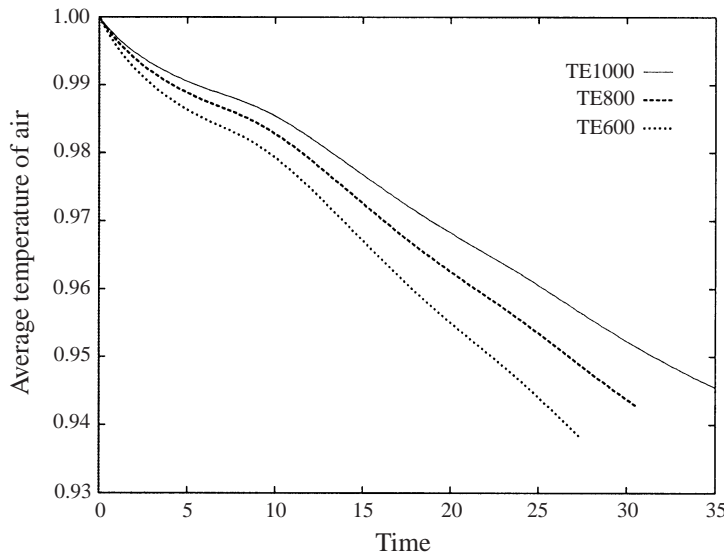FIGURE 12. Development of the thermodynamic pressure.

FIGURE 13. Development of the average air temperature.

The effect of thermal coupling on the spatially averaged air temperature is shown in figure 13. In general, the average air temperatures all decrease monotonically with time. It is clear that the rate of decrease is proportional to the level of thermal coupling. In other words, the higher the thermal coupling effect the lower the air temperature at any given instance. For every case, however, the rate of decrease of the average air temperature is slightly lower than that of the thermodynamic pressure. Note that for each case, the trends of evolution for the air temperature and for the thermodynamic pressure are very similar. Both have the highest rate of decrease at $T = 0$ and the lowest around $T = 7$ which corresponds to the rollup time. Since the rate of decrease is closely related to the thermal coupling effect, the lowest thermal

coupling effects occur around the rollup time. At $T = 0$, the droplets are distributed uniformly in the flow field and the temperature difference between the two phases is the largest, which gives rise to the highest thermal coupling effects. As the flow develops further, the droplets become concentrated in certain local areas owing to the Kelvin–Helmholtz rollups. This preferential dispersion of the droplets results in the lowest thermal coupling effects. The ensuing vortex pairing stretches the concentration area of the droplets which causes the thermal coupling effects to increase. However, the thermal coupling effect is generally lower during the pairing process than that at $T = 0$ because the temperature difference between the two phases is smaller and some residual areas of concentrated droplets remain in the flow field. It will be shown later that the droplets concentrate most during the rollup and produce the weakest thermal coupling effects compared to other periods.

The air temperature field across the mixing layer is also studied. Figure 14 shows the profile of $\bar{T}_c(y)$ at different times for the three two-way coupling cases. Here, $\bar{T}_c(y)$ is defined as

$$\bar{T}_c(y) = \frac{\int_{-L_x/2}^{L_x/2} \int_{-L_z/2}^{L_z/2} T_c(x, y, z) \mathrm{d}x\mathrm{d}z}{L_x L_z}. \tag{3.10}$$

At $T = 5$, because the droplets are still concentrated in the narrow region around $Y = 0$, the lowest value of $\bar{T}_c(y)$ occurs at $Y = 0$. When $T = 10$, the Kevin–Helmholtz rollups have developed and the droplets start to be thrown out by the large-scale vortex structures. So two local minimum values of $\bar{T}_c(y)$ occur near $Y = 0$. During the development of the vortex pairing (around $T = 20$), even more droplets have been thrown out and some droplets start to concentrate around $Y = 0$ in the mid-braid plane ($X = \pm L_x/2$) (Ling *et al.* 1998). Therefore, at $T = 20$, a local minimum value of $\bar{T}_c(y)$ again occurs and the profile of $\bar{T}_c(y)$ is broadened out. Finally, when $T = 30$, which is after the vortex pairing has taken place, the profile of $\bar{T}_c(y)$ is broadened even more. A case with higher thermal coupling effects always has a lower value of $\bar{T}_c(y)$ and the value of $\bar{T}_c(y)$ for all the three cases is less than unity for all time.

According to equation (2.1), the profile of $\bar{\rho}_c(y)$ should be similar to that of $\bar{T}_c(y)$ except that all the minimum or local minimum values should be maximum or local maximum values because P_0 is only a function of time. Here, $\bar{\rho}_c(y)$ is defined as

$$\bar{\rho}_c(y) = \frac{\int_{-L_x/2}^{L_x/2} \int_{-L_z/2}^{L_z/2} \rho_c(x, y, z) \mathrm{d}x\mathrm{d}z}{L_x L_z}. \tag{3.11}$$

The profiles of $\bar{\rho}_c(y)$ are shown in figure 15. The case with higher thermal coupling effects maintains higher values of $\bar{\rho}_c(y)$. While the value of $\bar{T}_c(y)$ is always less than unity, the value of $\bar{\rho}_c(y)$ can be greater than unity around $Y = 0$. The higher value of $\bar{\rho}_c(y)$ represents increased thermal contraction because of the higher droplet concentration. The thermal contraction around $Y = 0$ results in the increase in the magnitude of the vorticity and the largest effect at the earliest time causes the initial increase in $|\omega_z|_T$ shown in figure 6(*a*).

The details of the air temperature field can be compared with the distribution of the droplets. As an example, figure 16 shows the distribution of the droplets and the contours of the air temperature for case TE1000 on the $Z = 0$, $X = -L_x/2$, and $X = 0$ planes at $T = 23$, which is about the pairing time. For the distribution of the droplets, the plane actually represents a thin slice with a thickness of one computational cell centred at that position.
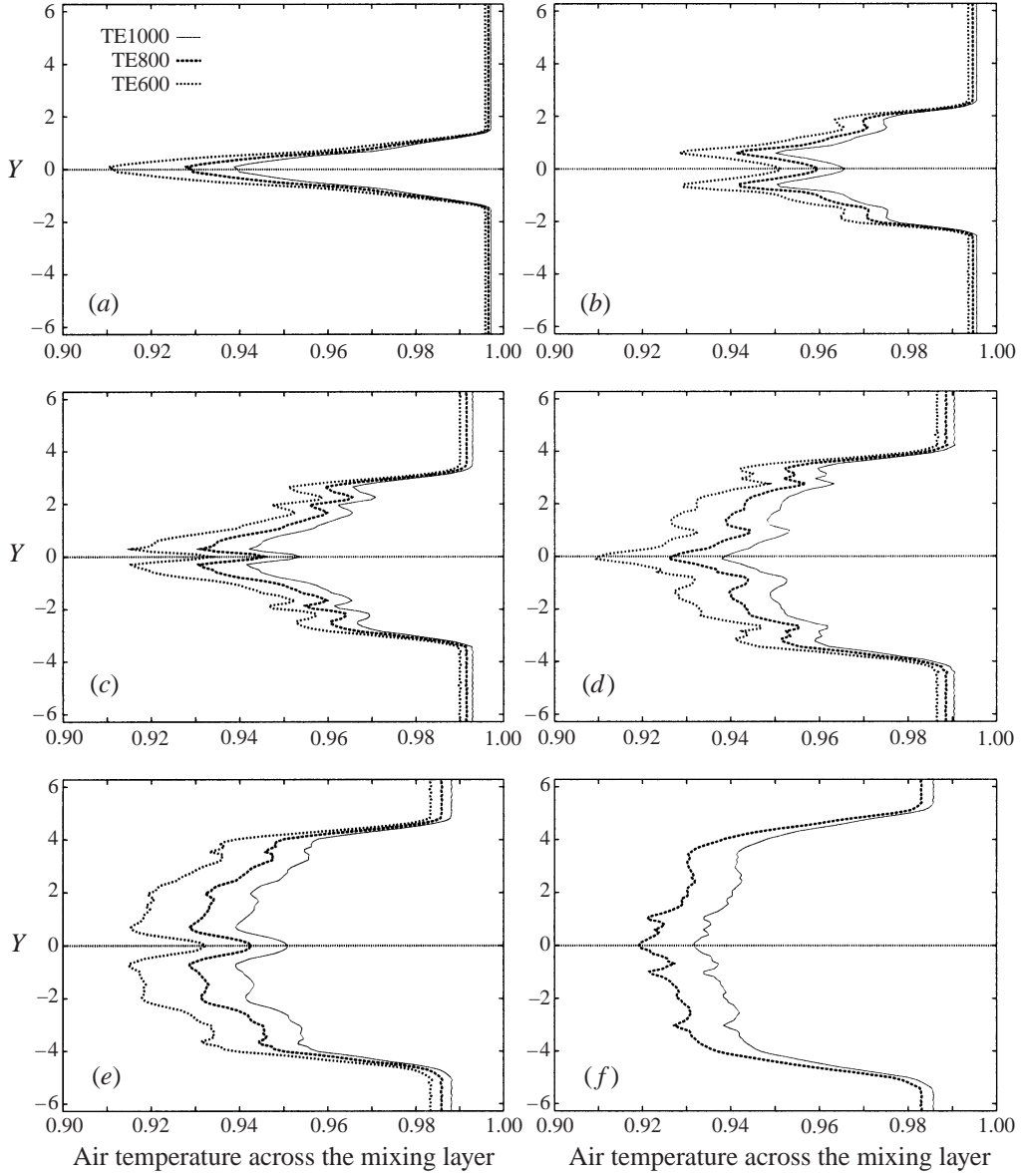
FIGURE 14. Profile of $\bar{T}_c(y)$ at (*a*) $T = 5$, (*b*) $T = 10$, (*c*) $T = 15$, (*d*) $T = 20$, (*e*) $T = 25$, (*f*) $T = 30$.

It is observed that the droplets still concentrate on the circumference of the large-scale vortex structures, and the counter-rotating rib structures cause the variation of the distribution of the droplets along the spanwise direction. On the $X = -L_x/2$ plane, the positions of lower air temperatures and positions of higher droplet concentration agree very well due to the low dispersion scale of both the fluid and droplets in this plane. However, on the $Z = 0$ plane, because the dispersion of both the fluid elements and droplets is orders of magnitude larger than those on the $X = -L_x/2$ plane, the location of the lower air temperatures depends on the history of the droplets and flow field. Therefore, they do not agree well with those of higher droplet concentrations.
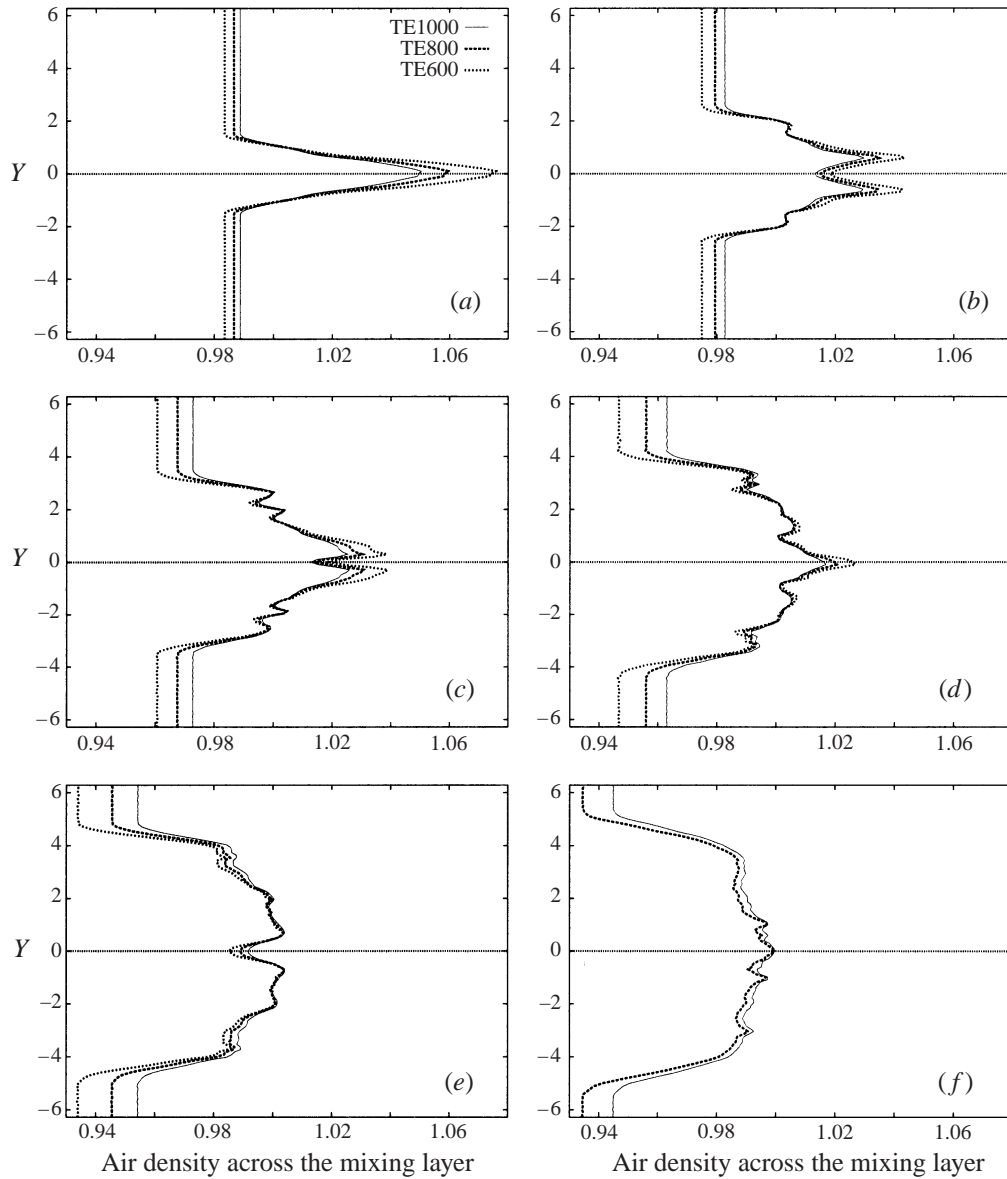
FIGURE 15. Profile of $\bar{\rho}_c(y)$ at (*a*) $T = 5$, (*b*) $T = 10$, (*c*) $T = 15$, (*d*) $T = 20$, (*e*) $T = 25$, (*f*) $T = 30$.

3.3. *Droplets*

While some qualitative results for the droplet dispersion are shown in figure 16, some quantitative results are addressed in this section.

Using the Lagrangian approach, the motion and evaporation of each droplet are computed. While the initial diameters of all the droplets are the same, the size of each droplet should be different at later time because it depends on the droplet path. As an example, figure 17 shows the size distribution of droplets for case TE800 at $T = 26$.

Because St_{mass}, the dimensionless mass response time of a droplet, is of order 10^3
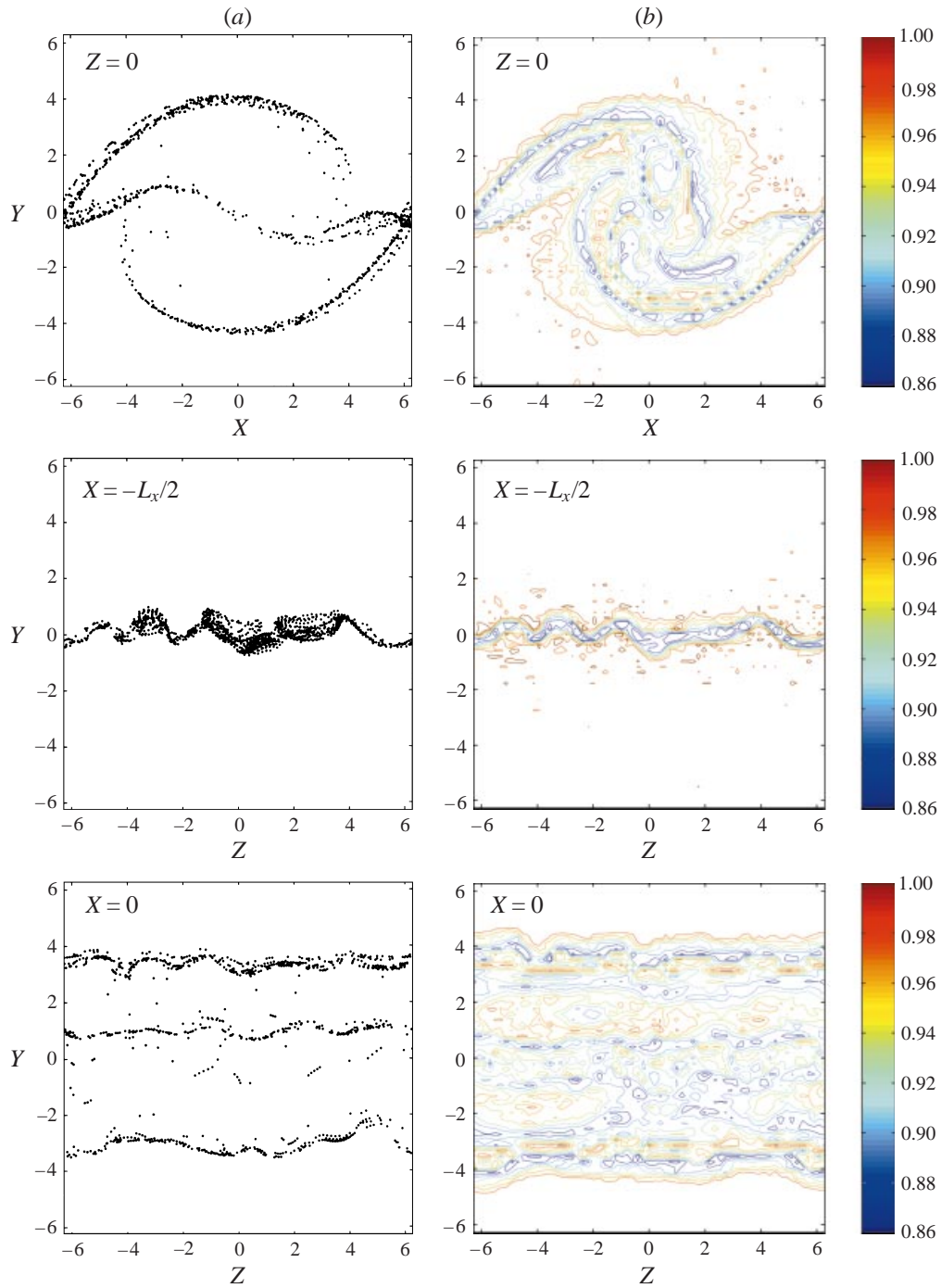
FIGURE 16. (*a*) Droplet distribution and (*b*) contours of air temperature for case TE1000 at $T = 23$.

for every case, which is orders of magnitude larger than the dimensionless time of the simulation, the change in droplet size is small. For example,the change in the average droplet Stokes number is less than 3%.

The change in the overall droplet concentration can be verified by studying the
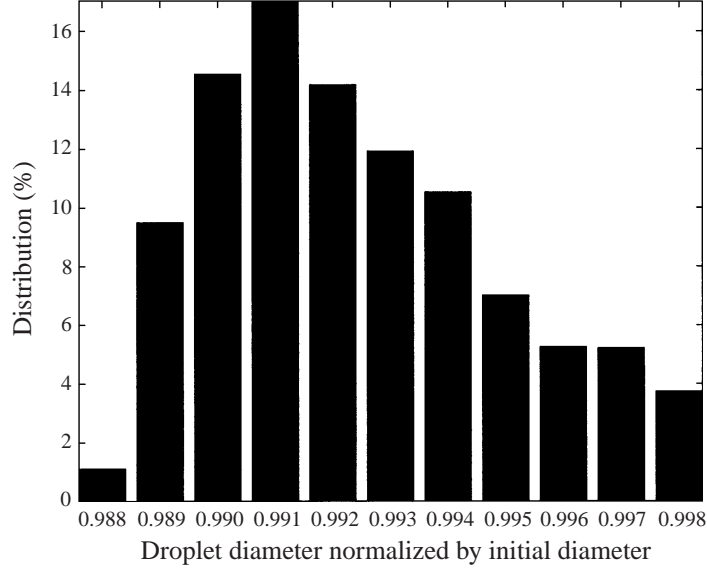
FIGURE 17. Droplet size distribution of case TE800 at $T = 26$.

development of N_{rms}, which is defined as

$$N_{rms} = \sqrt{\dfrac{\sum\limits_{i=1}^{N_c} N_i^2}{N_c}}, \qquad (3.12)$$

where N_c is total number of computational cells and N_i is the number of droplets in the ith cell. As shown in figure 18, the overall concentration of the droplets increases very fast initially and reaches a maximum value at time about 7. Then it starts to decrease due to the stretching effect of the vortex pairing and remains nearly constant for the time period from 10 to 20. Finally, it starts to increase again at a much lower rate than it does initially due to the folding effect after the vortex pairing. It is also seen that the overall concentration is higher for a case with higher thermal coupling because of the increased thermal contraction.

The dispersion scales of the droplets can be quantitatively studied by evaluating the dispersion function in the Y-direction for the droplets initially seeded on the $Y = 0$ plane and in Z-direction for the droplets initially seeded on the $Z = 0$ plane. These two dispersion functions are defined as

$$D_y(t) = \sqrt{\dfrac{1}{N_d} \sum_{i=1}^{N_p} (Y_i(t) - Y_m(t))^2}, \qquad (3.13)$$

$$D_z(t) = \sqrt{\dfrac{1}{N_d} \sum_{i=1}^{N_p} (Z_i(t) - Z_m(t))^2}, \qquad (3.14)$$

where N_d is the total number of droplets, $Y_m(t)$ is the mean value of droplet displacement in the transverse direction at time t, and $Z_m(t)$ is the mean value of droplets displacement in the spanwise direction at time t.
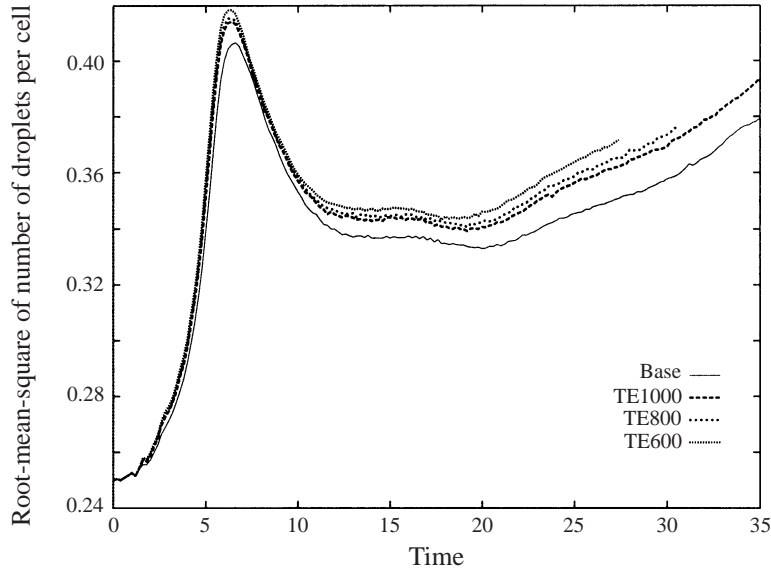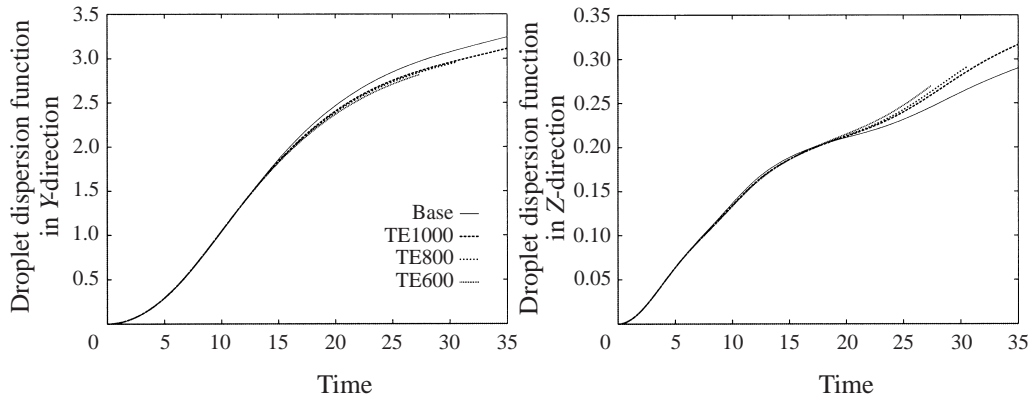
FIGURE 18. Development of N_{rms} for two-way thermal energy coupling cases.

FIGURE 19. Droplet dispersion function in (*a*) the *Y*-direction and (*b*) the *Z*-direction.

Figure 19(*a*) shows the dispersion function in the *Y*-direction and figure 19(*b*) shows the dispersion function in the *Z*-direction for all the three two-way thermal coupling cases with comparison to the base case. For the dispersion in the *Y*-direction, the case with higher thermal coupling has lower values because of the increased thermal contraction. For the dispersion in the *Z*-direction, the curves show a pivot point when time is about 18. The case with higher thermal coupling has lower values before this time and higher values after this time. This phenomenon is probably due to the combined effects of the thermal contraction, the droplet dispersion in both the *Y*- and *Z*-directions, and the increased magnitude of the vorticity.

4. Conclusions

Using the pseudo-spectral method and Lagrangian approach, three-dimensional two-way thermally coupled mixing layers with cool water droplets in hot air were

simulated. The flow was at low Mach number and the mass and momentum coupling effects were neglected because of low initial mass loading (< 0.1). The droplets were assumed to be at the wet-bulb temperature for all the time and represented as heat sinks in the flow. Initially, all droplets were at the Stokes number of 4 and distributed uniformly in a narrow region around the interface of the two streams. The initial Stokes number associated with the mass response time for the droplets is on the order of 10^3.

The following effects of the two-way thermal coupling were observed from the simulations.

(i) Evaporating droplets represent heat sinks in the flow, and the heat sinks result in a thermal contraction, a higher magnitude of the vorticity field, a higher overall droplet concentration and less droplet dispersion in the transverse direction.

(ii) At fixed initial conditions, the overall coupling effect at any time is directly related to the overall droplet concentration at that time. The highest droplet concentration corresponds to the lowest coupling effect.

(iii) The locations of lower air temperatures may not correspond to those of higher droplet concentrations because the dispersion history of both phases can play an important role.

Appendix. Approximation of the thermal energy equation for the air

Under the assumptions of void fraction near unity and no gravity, the thermal energy equation for the continuous phase can be approximated by

$$\frac{\partial(\rho_c i_c)}{\partial t} + \frac{\partial(\rho_c U_i i_c)}{\partial x_i} = -P\frac{\partial U_i}{\partial x_i} + \tau_{ij}\frac{\partial U_i}{\partial x_j} + S_m h_s + S_h. \tag{A 1}$$

Under the low Mach number assumption, the speed of sound is infinite and any disturbances in the thermodynamic pressure are felt instantaneously throughout the fluid. So, the thermodynamic pressure can only be a function of time in a closed domain. The dynamic pressure associated with the fluid motion, under order of magnitude analysis, does not participate directly in the thermal process (McMurtry *et al.* 1986). Therefore, the thermal energy equation (A 1) can be approximated by

$$\frac{\partial(\rho_c i_c)}{\partial t} + \frac{\partial(\rho_c U_i i_c)}{\partial x_i} = -P_0\frac{\partial U_i}{\partial x_i} + \tau_{ij}\frac{\partial U_i}{\partial x_j} + S_m h_s + S_h. \tag{A 2}$$

Using $i_c = C_v T_c$ and assuming C_v is constant due to the low mass loading, the thermal energy equation can be written as

$$C_v T_c\frac{\mathrm{D}\rho_c}{\mathrm{D}t} + C_v\rho_c\frac{\mathrm{D}T_c}{\mathrm{D}t} + C_v\rho_c T_c\frac{\partial U_i}{\partial x_i} = -P_0\frac{\partial U_i}{\partial x_i} + \tau_{ij}\frac{\partial U_i}{\partial x_j} + S_m h_s + S_h. \tag{A 3}$$

Neglecting mass loading effects, the mass continuity equation for the continuous phase is

$$\frac{\partial\rho_c}{\partial t} + \frac{\partial(\rho_c U_i)}{\partial x_i} = 0. \tag{A 4}$$

From the above equation, one has

$$\frac{\partial U_i}{\partial x_i} = -\frac{1}{\rho_c}\frac{\mathrm{D}\rho_c}{\mathrm{D}t}. \tag{A 5}$$

Substituting equation (A 5) into the left-hand side of the thermal energy equation

(A 3), one obtains

$$\rho_c C_v \frac{\mathrm{D}T_c}{\mathrm{D}t} = -P_0 \frac{\partial U_i}{\partial x_i} + \tau_{ij} \frac{\partial U_i}{\partial x_j} + S_m h_s + S_h. \tag{A 6}$$

Again, under order of magnitude analysis, $\tau_{ij}\partial U_i/\partial x_j$ is scaled by the ratio of the Eckert number to the Reynolds number and $S_m h_s$ is scaled by the reciprocal of τ_m. Therefore, both terms can be neglected for low Mach number and large τ_m. The final form of the thermal energy equation is

$$\rho_c C_v \frac{\mathrm{D}T_c}{\mathrm{D}t} = -P_0 \frac{\partial U_i}{\partial x_i} + S_h. \tag{A 7}$$

REFERENCES

BALACHANDAR, S. & MAXEY, M. R. 1989 Methods for evaluating fluid velocities in spectral simulations of turbulence. *J. Comput. Phys.* **83**, 96–125.

BERLEMONT, A., GRANCHER, M. S. & GOUESBET, G. 1995 Heat and mass transfer coupling between vaporizing droplets and turbulence using a Lagrangian approach. *Intl J. Heat Mass Transfer* **38**, 3023–3034.

BOIVIN, M., SIMONIN, O. & SQUIRES, K. D. 1998 Direct numerical simulation of turbulence modulation by particles in isotropic turbulence. *J. Fluid Mech.* **375**, 235–263.

BREIDENTHAL, R. E. 1978 A chemically reacting turbulent shear layer. PhD thesis California Institute of Technology.

BROWAND, F. K. & TROUTT, T. R. 1980 The turbulent mixing layer: geometry of large vortices. *J. Fluid Mech.* **158**, 489–509.

CHUNG, J. N. & TROUTT, T. R. 1988 Simulation of particle dispersion in an axisymmetric jet. *J. Fluid Mech.* **186**, 199–222.

CROWE, C. T., CHUNG, J. N. & TROUTT, T. R. 1988 Particle mixing in free shear flows. *Prog. Energy Combust. Sci.* **14**, 171–194.

CROWE, C. T., SOMMERFELD, M. & TSUJI, Y. 1997 *Multiphase Flows with Droplets and Particles.* CRC Press.

CROWE, C. T., TROUTT, T. R. & CHUNG, J. N. 1996 Numerical models for two-phase turbulent flows. *Ann. Revi. Fluid Mech.* **28**, 11–43.

EATON, J. K. & FESSLER, J. R. 1994 Preferential concentration of particles by turbulence. *Intl J. Multiphase Flow* **20**, 169–209.

EATON, J. K. & ROUSON, D. W. I. 1998 Particle interaction models for higher order simulations of particle-laden turbulence. *Proc. ICMF'98 Third Intl Conf. on Multiphase flow, Lyon, France, 1998.*

ELGHOBASHI, S. & TRUESDELL, G. C. 1993 On the two-way interaction between homogeneous turbulence and dispersed solid particles. I: Turbulence modification. *Phys. Fluids* A **3**, 1791–1801.

GORE, R. A. & CROWE, C. T. 1991 Modulation of turbulence by a dispersed phase. *Trans. ASME: J. Fluids Engng* **113**, 304–307.

HO, C. M. & HUERRE, P. 1984 Perturbed free shear layer. *Ann. Rev. Fluid Mech.* **16**, 365–424.

HUANG, L.-S. & HO, C.-M. 1990 Small-scale Transition in a Plane Mixing Layer. *J. Fluid Mech.* **290**, 475–500.

KIGER, K. T. & LASHERAS, J. C. 1995 The effect of vortex pairing on particle dispersion and kinetic energy transfer in a two-phase turbulent shear layer. *J. Fluid Mech.* **302**, 149–178.

LASHERAS, J. C., CHO, J. S. & MAXWORTHY, T. 1986 On the origin and evolution of streamwise vortical structures in a plane free shear flow. *J. Fluid Mech.* **172**, 231–258.

LASHERAS, J. C. & CHOI, H. 1988 Three-dimensional instability of a plane free shear layer: an experimental study of the formation and evolution of streamwise vortices. *J. Fluid Mech.* **189**, 53–88.

LING, W., CHUNG, J. N., TROUTT, T. R. & CROWE, C. T. 1998 Direct numerical simulation of a three-dimensional temporal mixing layer with particle dispersion. *J. Fluid Mech.* **358**, 61–85.

MARCU, B. & MEIBURG, E. 1996 Three-dimensional features of particle dispersion in a nominally plane mixing layer. *Phys. Fluids* **8**, 2266–2268.

MASHAYEK, F. 1998*a* Droplet-turbulence interactions in low-Mach-number homogeneous shear two-phase flows. *J. Fluid Mech.* **367**, 163–203.

MASHAYEK, F. 1998*b* Direct numerical simulations of evaporating droplet dispersion in forced low Mach number turbulence. *Intl J. Heat Mass Transfer* **41**, 2601–2617.

MCMURTRY, P. A., JOU, W.-H., RILEY, J. J. & METCALFE, R. W. 1986 Direct Numerical Simulations of a Reacting Mixing Layer with Chemical Heat Release. *AIAA J.* **24**, 962–970.

MCMURTRY, P. A., RILEY, J. J. & METCALFE, R. W. 1989 Effects of heat release on the large-scale structure in turbulent mixing layers. *J. Fluid Mech.* **199**, 297–332.

METCALFE, R. W., ORSZAG, S. A., BRACHET, M., MENON, S. & RILEY, J. J. 1987 Secondary instability of a temporally growing mixing layer. *J. Fluid Mech.* **184**, 207–243.

MICHAEL, D. H. 1965 Kelvin-Helmholtz instability of a dusty gas. *Proc. Camb. Phil. Soc.* **61**, 569–571.

MICHALKE, A. 1964 On the inviscid instability of the hyperbolic tangent velocity profile. *J. Fluid Mech.* **19**, 543–556.

MIKSAD, R. W. 1972 Experiments on the nonlinear stages of free shear layer transition. *J. Fluid Mech.* **56**, 695–719.

MOSER, R. D. & ROGERS, M. M. 1993 The three-dimensional evolution of a plane mixing layer. Part 2. Pairing and transition to turbulence. *J. Fluid Mech.* **247**, 275–320.

PIERREHUMBERT, R. T. & WIDNALL, S. E. 1982 The two- and three-dimensional instabilities of a spatially periodic shear layer. *J. Fluid Mech.* **114**, 59–82.

SAFFMAN, P. G. 1962 On the stability of laminar flow of a dusty gas. *J. Fluid Mech.* **13**, 120–128.

SQUIRES, K. D. & EATON, J. K. 1990 Particle response and turbulence modification in isotropic turbulence. *Phys. Fluids* A **2**, 1191–1203.

TANG, L., CROWE, C. T., CHUNG, J. N. & TROUTT, T. R. 1989 Effect of momentum coupling on the development of shear layers in gas-particle mixtures. In *Proc. Intl Conf. on Mechanics of Two-Phase Flows, Taipei, Taiwan, 1989*, pp. 387–391.

TATSUMI, T., GOTOH, K. & AYUKAWA, K. 1964 The stability of a free boundary layer at large Reynolds numbers. *J. Phys. Soc. Japan* **19**, 1966–1980.

TONG, X. L. & WANG, L. P. 1997 Direct simulations of particle transport in two and three dimensional mixing layers. *ASME Fluids Engineering Division Summer Meeting, 1997, Publication FEDSM'97-3635.*

TONG, X. L. & WANG, L. P. 1998*a* Two-way coupled particle-laden mixing layer. Part 1. Linear instability. *ASME Fluids Engineering Division Summer Meeting, 1998, Publication FEDSM'98-5032.*

TONG, X. L. & WANG, L. P. 1998*b* Two-way coupled particle-laden mixing layer. Part 2. Nonlinear evolution. *Proc. ICMF'98 Third Intl Conf. on Multiphase Flow, Lyon, France, 1998.*

WYGNANSKI, I., OSTER, D., FIEDLER, H. & DZIOMBA, B. 1979 On the perseverance of a quasi-two-dimensional eddy-structure in a turbulent mixing Layer. *J. Fluid Mech.* **93**, 325–336.

XU, C. G., CROWE, C. T., TROUTT, T. R. & CHUNG, J. N. 1998 Effect of mass and thermal coupling on bluff-body wake flows. *Proc. Third Intl Conf. on Multiphase Flow, ICMF'98.*

YANG, Y. Q., CHUNG, J. N., TROUTT, T. R. & CROWE, C. T. 1990 The influence of particles on the spatial stability of two-phase mixing layers. *Phys. Fluids* **2**, 1839–1845.